

# Quantitative analysis of two-band $\mathbf{k} \cdot \mathbf{p}$ models describing the shift-current photoconductivity

Julen Ibañez-Azpiroz,<sup>1</sup> Fernando de Juan,<sup>2,3</sup> and Ivo Souza<sup>1,2</sup>

<sup>1</sup>*Centro de Física de Materiales, Universidad del País Vasco (UPV/EHU), 20018 San Sebastián, Spain*

<sup>2</sup>*Ikerbasque Foundation, 48013 Bilbao, Spain*

<sup>3</sup>*Donostia International Physics Center (DIPC), 20018 San Sebastián, Spain*

(Dated: April 13, 2022)

We present a quantitative study of a two-band  $\mathbf{k} \cdot \mathbf{p}$  model and its description of several electronic and optical properties of monolayer BC<sub>2</sub>N and GeS, including the shift-current photoconductivity. Our analysis is based on a recently developed Wannier-interpolation scheme. Our results show that, while the band structure, joint density of states and dielectric function are accurately described by the  $\mathbf{k} \cdot \mathbf{p}$  model, it entails a significant error in the case of the shift current. We attribute the origin of this error to an approximation that is implicit in the tight-binding formulation, namely discarding off-diagonal position matrix elements. Our results thus highlight the strong sensitivity of the shift-current mechanism to wavefunction-properties.

## I. INTRODUCTION

Quick and efficient conversion of light into electricity is key for future clean-energy technologies. Recently a focus of renewed attention, the bulk photovoltaic effect (BPVE) is a nonlinear absorption process that converts light into electrical current intrinsically, *i.e.* without the need of any *pn*-junction for driving the photoexcited electrons. The BPVE can furthermore surpass the Shockley-Queisser limit for the solar-cell efficiency [1], thus opening the way for devices largely exceeding current capabilities. Alongside, the photovoltage attained in the BPVE is not limited by the band gap of the material, giving rise to huge measured values [2, 3].

In the last years, the study of the BPVE, and in particular the shift-current contribution, has witnessed a huge progress. This has led to groundbreaking discoveries including large nonlinear photovoltages achieved in Weyl semimetals [3, 4], a magnetically switchable light-matter interaction [5], nanotubes exhibiting orders of magnitude enhancement in the measured photovoltage as compared to the mono- and multi-layer value [6], and even the birth of an extremely promising variant effect, the so-called flexo-photovoltaic effect that turns widely used semiconductors like silicon into nonlinear photoelectrics [7].

The discovery of many of the aforementioned effects has been boosted by theoretical work. For instance, both model and first-principles calculations have emphasized the connection between topology and the sharp enhancement of the shift current [8–11]. Low-dimensional compounds such as one-dimensional polymer chains [12] and monochalcogenide single-layers [13] have also been recently investigated theoretically, showing an acute enhancement of the nonlinear response that is intimately linked to the properties of the electronic density of states [14]. Graphitic BC<sub>2</sub>N constitutes another recent example, where theoretical calculations have predicted a large and highly directional band-edge optical response governed by dipole selection rules [15].

The shift current has a marked quantum nature owing

to its strong sensitivity to wavefunction-properties, which makes it an appropriate platform for exploring new phenomena beyond the standard band-structure viewpoint. In a simplified picture, the shift current can be thought of as a real-space shift of the electron's center of mass resulting from the photoexcitation process between the valence and conduction bands in an acentric crystal. As a consequence, the localization properties of the wavefunction become particularly important for describing this mechanism. As noticed by recent works [16, 17], this may represent a problem for the widely used tight-binding model viewpoint, which discards off-diagonal elements of the position operator and hence important real-space information may be lost. In the prototypical material GaAs, for instance, this approximation entails a relative error of  $\sim 50\%$  on predicting the magnitude of the BPVE photoconductivity [16].

In this paper we perform a quantitative study of the quality of a two-band  $\mathbf{k} \cdot \mathbf{p}$  model in describing several electronic and optical properties, including the shift-current photoconductivity. We have chosen monolayer BC<sub>2</sub>N and GeS as a case studies due to their two-dimensional (2D) nature, which is shared by recent  $\mathbf{k} \cdot \mathbf{p}$  models proposed in the literature [14, 18]. For our analysis, we have made use of a recently developed *ab-initio* scheme [16] based on maximally localized Wannier functions (MLWFs) [19, 20]. Our results show that, while the band structure, joint density of states and dielectric function are accurately described by the  $\mathbf{k} \cdot \mathbf{p}$  model, it entails a significant error in the case of the shift current. We connect the origin of this error to an approximation implicitly assumed in the tight-binding formulation that amounts to discarding off-diagonal position matrix elements.

The paper is organized as follows. In Sec. II, we review the basic expressions of linear and nonlinear optical properties and their calculation via Wannier interpolation. In Sec. III, we provide the computational details of our *ab-initio* calculations. In Sec. IV we present and analyze our *ab-initio* and  $\mathbf{k} \cdot \mathbf{p}$  model results on the electronic

and optical properties of monolayer BC<sub>2</sub>N and GeS. A discussion of the results is included in Sec. V. Finally, in Appendix A we provide the technical steps that connect quasi-degenerate perturbation theory with the Wannier formulation, which is used for the numerical analysis of the two-band  $\mathbf{k} \cdot \mathbf{p}$  model throughout the main text.

## II. THEORETICAL FRAMEWORK

### A. Definitions

Consider a monochromatic electric field of the form

$$\mathcal{E}(t) = \mathcal{E}(\omega)e^{-i\omega t} + \mathcal{E}(-\omega)e^{i\omega t}, \quad (1)$$

with  $\mathcal{E}(-\omega) = \mathcal{E}^*(\omega)$ . The associated *dc* photocurrent density from the linear BPVE reads [21–23]

$$j^a = 2\sigma^{abc}(0; \omega, -\omega) \text{Re} [\mathcal{E}_b(\omega)\mathcal{E}_c(-\omega)]. \quad (2)$$

From Ref. 24, the interband (shift-current) part of the response is given by

$$\begin{aligned} \sigma^{abc}(0; \omega, -\omega) &= \frac{i\pi|e|^3}{4\hbar^2} \int [d\mathbf{k}] \sum_{n,m} f_{nm} (I_{mn}^{abc} + I_{mn}^{acb}) \\ &\times [\delta(\omega_{mn} - \omega) + \delta(\omega_{nm} - \omega)]. \end{aligned} \quad (3)$$

Above,  $f_{nm} = f_n - f_m$  and  $\hbar\omega_{nm} = E_m - E_n$  are differences between occupation factors and band energies, respectively, and the integral is over the first Brillouin zone, with  $[d\mathbf{k}] = d^d k / (2\pi)^d$  in  $d$  dimensions. The transition matrix element is given by

$$I_{mn}^{abc} = r_{mn}^b r_{nm}^{c;a}, \quad (4)$$

with

$$r_{\mathbf{k}nm}^a = (1 - \delta_{nm}) A_{\mathbf{k}nm}^a \quad (5)$$

the interband dipole matrix, and

$$r_{\mathbf{k}nm}^{a;b} = \partial_b r_{\mathbf{k}nm}^a - i (A_{\mathbf{k}nn}^b - A_{\mathbf{k}mm}^b) r_{\mathbf{k}nm}^a \quad (6)$$

its “generalized derivative”. In the above expressions,

$$A_{\mathbf{k}nm}^a = i \langle u_{\mathbf{k}n} | \partial_a u_{\mathbf{k}m} \rangle \quad (7)$$

denotes the Berry connection matrix, with  $|u_{\mathbf{k}m}\rangle$  the cell-periodic part of a Bloch eigenstate and  $\partial_a$  stands for  $\partial/\partial k_a$ .

For comparison purposes throughout the work, let us define two further quantities: the joint density of states (JDOS) per crystal cell,

$$N(\omega) = \frac{v_c}{\hbar} \int [d\mathbf{k}] \sum_{n,m} f_{nm} \delta(\omega_{mn} - \omega) \quad (8)$$

( $v_c$  is the cell volume), and the interband contribution to the absorptive (abs) part of the dielectric function [24],

$$\epsilon_{\text{abs}}^{ab}(\omega) = \frac{i\pi e^2}{\hbar} \int [d\mathbf{k}] \sum_{n,m} f_{nm} K_{nm}^{ab} \delta(\omega_{mn} - \omega), \quad (9)$$

with the transition matrix-elements given by

$$K_{nm}^{ab} = r_{nm}^a r_{mn}^b. \quad (10)$$

In nonmagnetic crystals  $\epsilon_{\text{abs}}^{ab}$  is purely imaginary and symmetric, and we report values for  $\text{Im} \epsilon_{\text{r}}^{ab} = \text{Im} \epsilon_{\text{abs}}^{ab} / \epsilon_0$ , the imaginary part of the relative permittivity.

### B. Wannier interpolation

Wannier functions are expressed as [25]

$$|\mathbf{R}j\rangle = v_c \int [d\mathbf{k}] e^{i\mathbf{k}\cdot(\hat{\mathbf{r}} - \mathbf{R} - \boldsymbol{\tau}_j)} |u_{\mathbf{k}j}^{(W)}\rangle \quad (11)$$

where  $|u_{\mathbf{k}j}^{(W)}\rangle$  stand for “Wannier-gauge” Blochlike states; these are related to “Hamiltonian-gauge” Bloch states  $|u_{\mathbf{k}m}\rangle$  by a  $M \times M$  rotation matrix  $U_{\mathbf{k}nj}$ :

$$|u_{\mathbf{k}j}^{(W)}\rangle = \sum_{j=1}^M |u_{\mathbf{k}m}\rangle U_{\mathbf{k}nj}. \quad (12)$$

Note that we included the Wannier center

$$\boldsymbol{\tau}_j = \langle \mathbf{0}j | \hat{\mathbf{r}} | \mathbf{0}j \rangle \quad (13)$$

in the phase factor of Eq. (11), following the phase convention in Ref. 26.

Wannier interpolation is a Slater-Koster type of interpolation, with the Wannier functions acting as an orthogonal tight-binding basis [25]. This has been shown to provide a smooth  $k$ -space interpolation of several quantities [27]. As an example, *ab-initio* eigenvalues can be Wannier-interpolated by considering the matrix elements of the first-principles Hamiltonian  $\hat{H}_{\mathbf{k}} = e^{-i\mathbf{k}\cdot\hat{\mathbf{r}}} \hat{H} e^{i\mathbf{k}\cdot\hat{\mathbf{r}}}$  between the Blochlike states of Eq. (12):

$$\begin{aligned} H_{\mathbf{k}ij}^{(W)} &= \langle u_{\mathbf{k}i}^{(W)} | \hat{H}_{\mathbf{k}} | u_{\mathbf{k}j}^{(W)} \rangle \\ &= \sum_{\mathbf{R}} e^{i\mathbf{k}\cdot(\mathbf{R} + \boldsymbol{\tau}_j - \boldsymbol{\tau}_i)} \langle \mathbf{0}i | \hat{H} | \mathbf{R}j \rangle. \end{aligned} \quad (14)$$

Diagonalization of this  $M \times M$  matrix yields the Wannier-interpolated energy eigenvalues,

$$\left( U_{\mathbf{k}}^\dagger H_{\mathbf{k}}^{(W)} U_{\mathbf{k}} \right)_{nm} = E_{\mathbf{k}n} \delta_{nm}. \quad (15)$$

As described in Appendix A, the above quantities,  $H_{\mathbf{k}ij}^{(W)}$  and  $E_{\mathbf{k}n}$ , can be used for constructing a Wannier-based  $\mathbf{k} \cdot \mathbf{p}$  model via quasi-degenerate perturbation theory.

In addition to the eigenvalues, Wannier-interpolation has been shown to provide an efficient method for interpolating the linear optical conductivity involving the position matrix element in Eq. (5) [27, 28], and more recently nonlinear properties involving the generalized derivative in Eq. (6) [16, 17]. In this work, we follow the approach presented in Ref. 16 and currently implemented into the new version of the **Wannier90** code package [29] for the calculation of the shift-current conductivity in Eq. (3).

### III. COMPUTATIONAL DETAILS

We have performed density-functional theory calculations using the Quantum ESPRESSO code package [30]. We treated the core-valence interaction using scalar-relativistic projector augmented-wave pseudopotentials available at the Quantum ESPRESSO website. The pseudopotentials were generated with the Perdew-Burke-Ernzerhof exchange-correlation functional [31], while the energy cutoff for the plane-wave basis expansion was set at 70 Ry. In a postprocessing step, we generated maximally-localized Wannier functions [19, 20] via the Wannier90 code package [32]. Finally, the shift-current spectrum [Eq. (3)], the JDOS [Eq. (8)], and the dielectric function [Eq. (9)] were calculated using Wannier interpolation.

In order to model the properties of monolayer BC<sub>2</sub>N, we used a slab geometry with a supercell of length  $l = 20$  Å along the nonperiodic direction. We took the in-plane structural parameters from Ref. 33, with lattice vectors  $\mathbf{a}_1 = 2.46 \hat{x}$  Å and  $\mathbf{a}_2 = 4.32 \hat{y}$  Å. The  $k$ -point mesh used for the self-consistent calculation was  $10 \times 10 \times 1$ , while for the non-self-consistent one we used a  $15 \times 15 \times 1$  mesh. For the construction of MLWFs, we considered four different sets composed of 2, 4, 8 and 16 disentangled bands. For the initial projections, we used  $p_z$  orbitals centred at C atoms,  $p_z$  orbitals centred at every atom,  $p_z$  and  $p_x$  orbitals centred at every atom, and  $s$  and  $p$  orbitals centred at every atom for the sets composed of 2, 4, 8 and 16 bands, respectively. We employed a dense  $k$ -point interpolation grid of  $2000 \times 2000 \times 1$  in order to achieve a well-converged optical spectrum. For the integrals of Eq. (3), (8) and (9), we used a fixed width of 0.01 eV for the broadening of the delta function, as it was found to properly handle the van-Hove singularities characteristic of two-dimensional (2D) systems.

Following Ref. 14, we defined a 3D-like response using a stacking distance of  $d = \sqrt{\mathbf{a}_1^2 + \mathbf{a}_2^2} = 4.97$  Å and rescaled the calculated response of the slab of thickness  $l$  by

$$\sigma_{3D}^{abc} = \frac{l}{d} \sigma_{\text{slab}}^{abc}. \quad (16)$$

Throughout the work we report values for  $\sigma_{3D}^{abc}$  and omit the 3D subindex, using the notation of Sec. II. We use the same rescaling of Eq. (16) for the dielectric function.

Concerning monolayer GeS, we modelled it by considering the setup of our previous work in Ref. [16].

## IV. RESULTS

### A. Monolayer BC<sub>2</sub>N

The crystal structure of monolayer BC<sub>2</sub>N is shown in Fig. 1, which is composed of alternating zigzag chains of graphene and hexagonal boron nitride. Its space group is  $Pmm2$  (No. 25), and its point group is  $mm2$ . Inversion

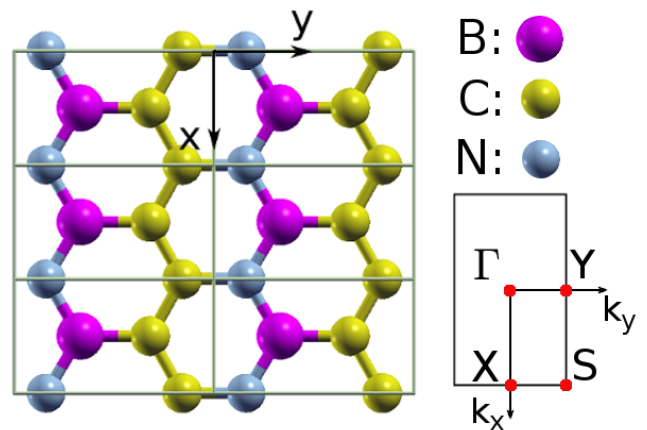


FIG. 1: Crystal structure and Brillouin zone of monolayer BC<sub>2</sub>N. The crystal structure includes two formula units per cell, with C, B and N atoms represented by yellow, blue and magenta balls respectively. The solid lines delimit the cells (the vertical lines coincide with one family of mirror planes).

symmetry is broken, and it contains two mirror planes,  $M_x$  and  $M_z$ , as well as a rotation  $C_2^y$  about the polar axis. Point-group symmetry allows five out of nine components of the linear BPVE tensor  $\sigma^{abc} = \sigma^{acb}$  to be nonzero: three involving in-plane directions only ( $yxx$ ,  $xyy = yxy$ , and  $yyy$ ), and two that also involve  $z$  ( $yzx$  and  $zzy = zyz$ ). For the sake of clarity, in this work we will restrict ourselves to analyzing only in-plane components with  $b = c$ , *i.e.*, the response to light polarized on the plane.

#### 1. Ab-initio properties

In Fig. 2(a) we show the dispersion near the band edge at S, with the direct band gap between valence ( $v$ ) and conduction ( $c$ ) bands plotted in Fig. 2(b). The minimum direct band gap is  $E_g \approx 1.6$  eV, which is in good agreement with previous calculations [33, 34]. The S-X line, and hence the band edge at S, remains invariant under both  $M_x$  and  $M_z$ , so that the energy eigenstates are also eigenstates of both mirror operators. This implies that the optical properties will be governed by dipole selection rules determined by the relative mirror eigenvalues of valence and conduction bands [15, 35, 36]. We calculated the mirror eigenvalues using the `irrep` computational package [37], which indicates that valence and conduction bands have *opposite* and *equal* mirror parities for  $M_x$  and  $M_z$ , respectively. This implies the dipole selection rule

$$r_{\mathbf{k}vc}^y = 0 \quad (17)$$

applies at the band edge. Monolayer BC<sub>2</sub>N therefore fulfils the same conditions as the noncentrosymmetric bulk polytype of the same material studied in Ref. 15.

We next turn to analyze the calculated optical properties, namely the nonlinear shift current [Eq. (3)] and lin-

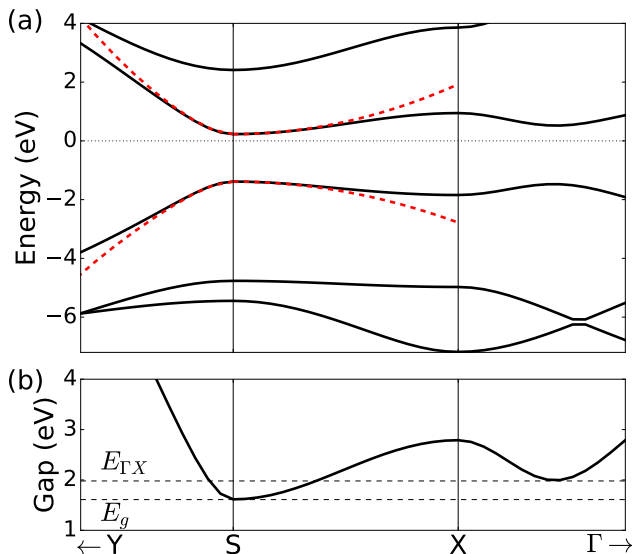


FIG. 2: Top: Dispersion near the band edge of single-layer  $\text{BC}_2\text{N}$ , with energies measured from the Fermi level. Red dashed lines denote the dispersion obtained from a two-band  $\mathbf{k}\cdot\mathbf{p}$  model expanded around the S point. Bottom:  $\mathbf{k}$ -resolved value of the direct band gap along the same paths as in (a).  $E_g$  denotes the band edge value while  $E_{\Gamma X}$  marks the energy difference between conduction and valence bands at the dispersion minima midway between  $\Gamma$  and  $X$ .

ear dielectric function [Eq. (9)]. In Fig. 3(a) we display the two symmetry-allowed components for light polarized on the plane, namely  $yxx$  and  $yyy$ . The maximum corresponds to the  $\sigma^{yxx} \sim 60 \mu\text{A}/\text{V}^2$  peak at  $\omega \sim 2.4$  eV, which is of the same order as the maximum shift current predicted for other 2D materials like monochalcogenides [13].  $\sigma^{yyy}$ , in turn, is significantly smaller than  $\sigma^{yxx}$  over all the shown frequency range. In the band-edge region spanning  $\sim [1.6, 2.0]$  eV,  $\sigma^{yyy}$  is virtually zero, as dictated by the dipole selection rule of Eq. (17) when plugged in the matrix element of Eq. (4). Note that the upper bound of the band-edge region,  $E_{\Gamma X} \sim 2$  eV, coincides with the onset of strong transitions from valence to conduction bands in the  $\mathbf{k}$ -space region lying midway between  $\Gamma$  and  $X$  points [c.f. Fig. 2]; since this is not a  $M_x$ -invariant line, dipole selection rules do not apply above  $E_{\Gamma X}$ . Contrary to  $\sigma^{yyy}$ ,  $\sigma^{yxx}$  is finite in the band-edge region and shows a step-like feature, reaching a plateau of  $\sim 5 \mu\text{A}/\text{V}^2$ .

Turning next to the linear dielectric function, the two symmetry-allowed in-plane components,  $xx$  and  $yy$ , are shown in Fig. 3(b). As in the case of the shift current,  $\text{Im} \epsilon_r^{ab}$  is also affected by the dipole selection rule of Eq. (17) via Eq. (10) in the band-edge region;  $\text{Im} \epsilon_r^{yy}$  is virtually null while  $\text{Im} \epsilon_r^{xx}$  is finite and shows a step-like feature. Overall, the shapes of  $\text{Im} \epsilon_r^{yy}$  and  $\text{Im} \epsilon_r^{xx}$  are reminiscent of those of  $\sigma^{yyy}$  and  $\sigma^{yxx}$ , respectively. This is in part due to the common position matrix element shared by both quantities, as it can be inferred from the compar-

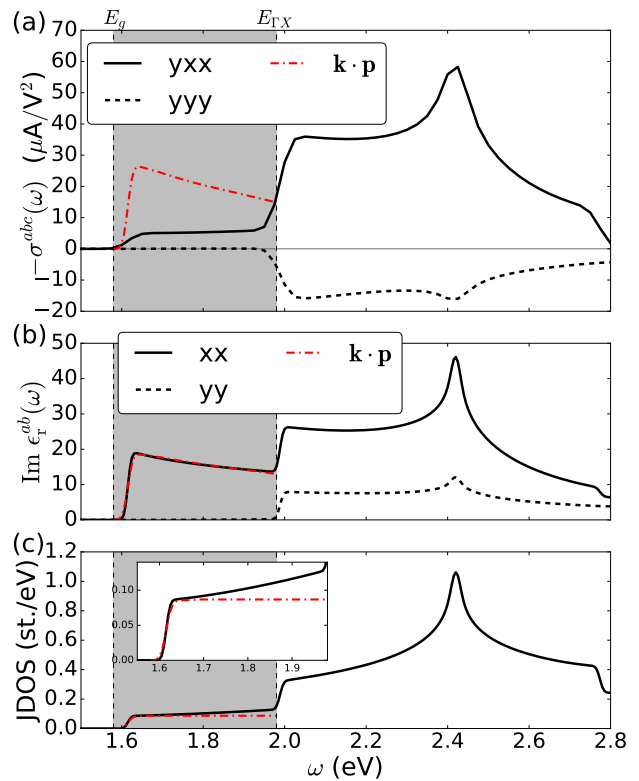


FIG. 3: (a) Shift-current spectrum, (b) imaginary part of the dielectric function, and (c) joint density of states of monolayer  $\text{BC}_2\text{N}$ . Black lines indicate *ab-initio* calculations, while the red lines depict the prediction of the two-band  $\mathbf{k}\cdot\mathbf{p}$  model. The grey area highlights the band-edge region from  $E_g \sim 1.6$  eV to  $E_{\Gamma X} \sim 2$  eV.

ison of Eqs. (4) and (10). Additionally, both quantities are related to the JDOS [compare Eqs. (3) and (9) with Eq. (8)], which is plotted in Fig. 3(c). It exhibits van-Hove-like singularities at  $E_g \sim 1.6$  eV and  $E_{\Gamma X} \sim 2$  eV, as well as a strong peak at  $\sim 2.4$  eV. Hence, the main features of both the shift current and the dielectric function are inherited from the behavior of the JDOS.

## 2. Two-band model

In this section, we construct a two-band  $\mathbf{k}\cdot\mathbf{p}$  model for reproducing the electronic and optical properties of monolayer  $\text{BC}_2\text{N}$ . This will serve to test the quality of the model in describing the different quantities. We report results calculated using a basis of 16 MLWFs, which were needed to converge the band summation of quasidegenerate perturbation theory (see Appendix A).

A two-band model expanded around a generic  $\mathbf{k}$ -point can be expressed in terms of Pauli matrices  $\sigma_i$  and the identity matrix  $\mathbb{1}$  as

$$\tilde{H}(\mathbf{k}) = \epsilon_0(\mathbf{k})\mathbb{1} + \sum_i f_i(\mathbf{k})\sigma_i \quad (i = x, y, z), \quad (18)$$

where  $\epsilon_0(\mathbf{k})$  and  $f_i(\mathbf{k})$  are real coefficients. The energies of the valence and conduction bands of this model are given by

$$\begin{aligned} E_v(\mathbf{k}) &= \epsilon_0(\mathbf{k}) - \epsilon(\mathbf{k}), \\ E_c(\mathbf{k}) &= \epsilon_0(\mathbf{k}) + \epsilon(\mathbf{k}), \end{aligned} \quad (19)$$

with  $\epsilon(\mathbf{k}) = \sqrt{f_i(\mathbf{k}) \cdot f_i(\mathbf{k})}$ .

By employing the Wannier-based quasi-degenerate perturbation theory outlined in Appendix A, we have constructed a two-band model expanded around the band-edge S. The corresponding band dispersion is shown in Fig. 2(a) as dashed lines. Comparison to the DFT band structure shows a nice quantitative agreement in the neighborhood of S, in line with what was found in a similar study in transition metal dichalcogenides [38].

In the following, we analyze the quality of the two-band  $\mathbf{k} \cdot \mathbf{p}$  model in quantitatively predicting the optical properties of monolayer BC<sub>2</sub>N. Our focus is on the band-edge region, where the shift current and the dielectric function take the form

$$\sigma_{\mathbf{k} \cdot \mathbf{p}}^{abc}(\omega) = I_{\mathbf{k} \cdot \mathbf{p}}^{abc}(\omega)N(\omega), \quad (20)$$

$$\epsilon_{\mathbf{k} \cdot \mathbf{p}}^{ab}(\omega) = K_{\mathbf{k} \cdot \mathbf{p}}^{ab}(\omega)N(\omega), \quad (21)$$

*i.e.*, at each frequency they are given by the product between the transition matrix-elements and the JDOS.

The expression for the shift-current matrix element for the generic two-band model of Eq. (18) was derived in Refs. 14 and 39, and reads

$$I_{\mathbf{k} \cdot \mathbf{p}}^{abc} = \sum_{ijm} \frac{1}{4\epsilon^3} [(f_m f_{i,b} f_{j,ac} - f_m f_{i,b} f_{j,a} \frac{\epsilon_{,c}}{\epsilon}) \epsilon_{ijm} + (b \leftrightarrow c)], \quad (22)$$

with  $\epsilon_{,a} = \partial_{k_a} \epsilon = \frac{1}{\epsilon} \sum_i f_i f_{i,a}$ ,  $f_{i,a} \equiv \partial_{k_a} f_i$ ,  $f_{i,ab} \equiv \partial_{k_a} \partial_{k_b} f_i$  and  $\epsilon_{ijm}$  the Levi-Civita symbol (we have omitted  $\mathbf{k}$ -labels for brevity). Similarly, the linear dielectric function of a generic two-band model can be derived from the expression of the linear conductivity reported in Ref. 18, and reads

$$K_{\mathbf{k} \cdot \mathbf{p}}^{ab}(\omega) = \sum_i \frac{4}{\epsilon^2} f_{i,a} f_{i,b}. \quad (23)$$

Using the extracted coefficients  $\epsilon_0(\mathbf{k})$  and  $f_i(\mathbf{k})$ , we have calculated the shift current [Eq. (20)] and dielectric function [Eq. (21)] within the two-band  $\mathbf{k} \cdot \mathbf{p}$  model, as well as the JDOS [Eq. (8)], for which only the energies of Eq. (19) are needed. The results have been included as dash-dotted lines in the band-edge region of Fig. 3.

Starting the analysis with the simplest quantity, the JDOS in Fig. 3(c), the comparison of the  $\mathbf{k} \cdot \mathbf{p}$  prediction to the *ab-initio* results shows a nearly perfect quantitative agreement in reproducing the height of the van-Hove-like singularity at  $E_g$ . Above the band gap energy, the *ab-initio* JDOS grows monotonically; this feature is not captured by the constant prediction of the model, but the discrepancy is rather small.

Turning next to the dielectric function in Fig. 3(b), the  $\mathbf{k} \cdot \mathbf{p}$  prediction for  $\epsilon_{\mathbf{k} \cdot \mathbf{p}}^{xx}$  matches very well the step-like feature present at the band-edge region in the *ab-initio* calculations, while  $\epsilon_{\mathbf{k} \cdot \mathbf{p}}^{yy} = 0$  for the model (not shown). Furthermore, the  $\mathbf{k} \cdot \mathbf{p}$  spectrum for  $\epsilon_{\mathbf{k} \cdot \mathbf{p}}^{xx}$  is able to reproduce the slight decrease of  $\text{Im} \epsilon_r^{xx}$  above  $E_g$  through the  $1/\epsilon^2$  factor in Eq. (23).

We finish our analysis turning to the shift current spectrum, which is shown in Fig. 3(a). In contrast to the JDOS and the dielectric function, the  $\mathbf{k} \cdot \mathbf{p}$  prediction for the shift-current component  $\sigma_{\mathbf{k} \cdot \mathbf{p}}^{yxx}$  at  $E_g$  overestimates the *ab-initio* result roughly by a factor five, while  $\sigma_{\mathbf{k} \cdot \mathbf{p}}^{yyy} = 0$  for the model (not shown). At larger energies within the band-edge region, the *ab-initio* result for the  $yxx$  component remains nearly constant whereas the  $\mathbf{k} \cdot \mathbf{p}$  prediction shows a marked monotonic decrease.

In conclusion, while the two-band  $\mathbf{k} \cdot \mathbf{p}$  model provides an accurate quantitative description of the band dispersion, JDOS and dielectric function of monolayer BC<sub>2</sub>N near the band-edge region, it fails in doing so for the shift current. A possible source for this failure is analyzed in the next section.

### 3. Diagonal tight-binding approximation

In this section, we analyze the quantitative effect of the so-called ‘‘diagonal tight-binding approximation’’ (diagonal TBA). This approximation is a customary postulate assumed implicitly in the tight-binding formulation [26, 40–43], which consists on discarding the off-diagonal elements of the position operator. The purpose of considering the diagonal TBA is to determine the extent of its effect for the quantitative prediction of the shift current. This is relevant for putting into context the results of the two-band  $\mathbf{k} \cdot \mathbf{p}$  model of Sec. IV A 2, which implicitly assumes this approximation.

In the notation of Sec. II, the diagonal TBA amounts to setting

$$\langle \mathbf{0}i | \hat{\mathbf{r}} | \mathbf{R}j \rangle \doteq \tau_i \delta_{\mathbf{R},0} \delta_{ji}, \quad (24)$$

where we have introduced the symbol ‘‘ $\doteq$ ’’ to denote equalities that only hold only within this approximation. The Wannier-based formalism outlined in Sec. II gives access to the matrix elements  $\langle \mathbf{0}i | \hat{\mathbf{r}} | \mathbf{R}j \rangle$ , hence it is suitable for analyzing the diagonal TBA through the implementation of Eq. (24). Furthermore, this analysis can be performed for different sizes of the MLWFs sets, *i.e.*, different number of basis states  $M$  entering Eq. (12).

We have considered four different sets including 2, 4, 8 and 16 states spanning the bands lying closest to the Fermi level in Fig. 2; the diagonal TBA results are compared with the exact one in Fig. 4a and Fig. 4b for the shift current and the dielectric function, respectively. Starting with the shift current, Fig. 4a reveals a large dependence of the diagonal TBA on the size of the basis set: the calculation with 2 MLWFs overestimates the

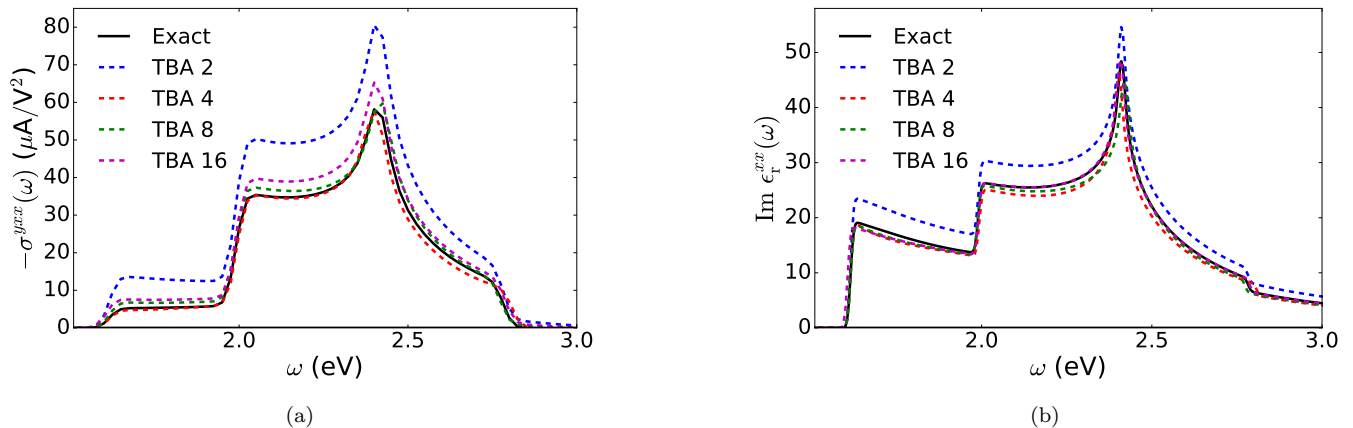


FIG. 4: Comparison between the exact result (solid line) and the outcome of the diagonal TBA as a function of the basis size (dashed lines) in BC<sub>2</sub>N: (a) for the  $xyx$  component of the shift current and (b) for the  $xx$  component of the dielectric function.

exact value by nearly 50%, the comparison improves significantly for the set with 4 MLWFs, but worsens for the calculations with 8 and 16 MLWFs, the later showing an appreciable relative error of up to 30% in the band-edge region. It is noteworthy that the results of the diagonal TBA for the shift current do not seem to converge with increasing size of the basis set. In comparison, the dielectric function in Fig. 4b is much less affected by the diagonal TBA: the calculation with 2 MLWFs is the only one showing an appreciable relative error of  $\sim 15\%$ , while the rest entail less than  $\sim 5\%$  relative error.

In order to gain a deeper insight into the nature of the diagonal TBA, we next analyze its effect on the  $k$ -resolved shift-current matrix-element summed over the

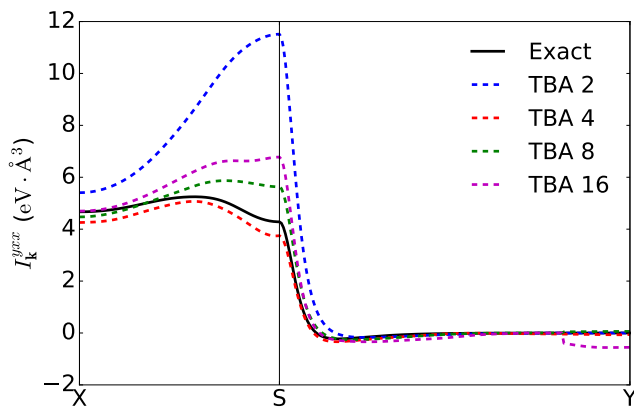


FIG. 5:  $k$ -resolved plot of the shift-current matrix-element of Eq. (25) for the  $yxx$  component in BC<sub>2</sub>N. The path covers the X–S–Y line in the BZ. The solid line denotes the exact result, while the dashed lines denote the results of the diagonal TBA including different amount of MLWFs into the basis set.

valence and conduction bands:

$$I_{\mathbf{k}}^{abc} = \frac{i\pi|e|^3}{2\hbar^2} \sum_{n,m}^{v,c} f_{nm} I_{mn}^{abc}. \quad (25)$$

Results for the  $yxx$  component are shown in Fig. 5 along the X–S–Y path. This figure again reveals a large dependence on basis-size, which is furthermore  $k$ -dependent; while in much of the S–Y line the diagonal TBA is close to the exact value, at the band-edge point S it can be off by as much as a factor 3. We leave the discussion of these results for Sec. V.

## B. GeS

GeS is a monochalcogenide belonging to the group IV. The members of this family are centrosymmetric in bulk form, but become polar – and therefore piezoelectric – when synthesized as a monolayer. The space group of monolayer GeS is  $Pnma$ , and the point group is  $mm2$ , *i.e.*, it shares the same point group as BC<sub>2</sub>N. As analyzed in Sec. IV A, this point group allows for five independent components of the shift-current conductivity tensor to be finite. In order to facilitate comparison with the results of Sec. IV A, we define the coordinate axes for monolayer GeS by replacing  $x \rightarrow z$ ,  $y \rightarrow x$  and  $z \rightarrow y$  as compared to the coordinate axes used in Ref. 13. In this way, the mirror planes, the ferroelectric polarization axis, and the nonzero shift-current components become the same as those in Sec. IV A.

### 1. Ab-initio properties

The electronic and optical *ab-initio* properties of monolayer GeS where studied in depth in Ref. 13. Here we present and discuss the properties that facilitate the ensuing discussion.

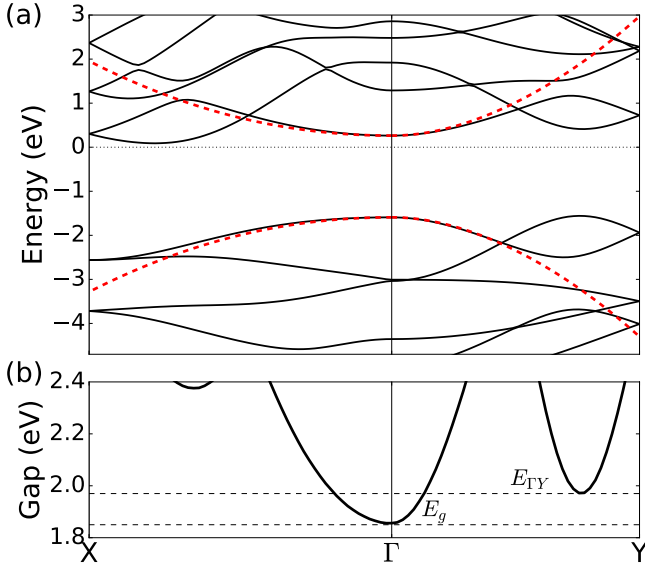


FIG. 6: Top: Dispersion near the band edge of monolayer GeS, with energies measured from the Fermi level. Red dashed lines denote the dispersion obtained from a two-band  $\mathbf{k} \cdot \mathbf{p}$  model expanded around the  $\Gamma$  point. Bottom:  $\mathbf{k}$ -resolved value of the direct band gap along the same paths as in (a).  $E_g$  denotes the band edge value while  $E_{\Gamma Y}$  marks the energy difference between conduction and valence bands at the dispersion minima midway between  $\Gamma$  and  $Y$ .

The calculated band structure [Fig. 6(a)] shows that the minimum direct band gap of  $E_g \sim 1.83$  eV takes place at the  $\Gamma$  point, which is invariant under both  $M_x$  and  $M_z$  mirror symmetries. The calculated mirror eigenvalues [37] indicate that valence and conduction bands have *equal* mirror parities for both mirror operators. This, in turn, implies that the dipole selection rule

$$r_{\mathbf{k}vc}^x = 0 \quad (26)$$

applies at the band edge [15, 35, 36]. Note that this is different to the dipole selection rule applying to monolayer  $\text{BC}_2\text{N}$  [Eq. (17)].

The dipole selection rule of Eq. (26) manifests in the optical properties close to the band edge, shown in Fig. 7. Fig. 7(a) shows the two symmetry-allowed components for the shift current under in-plane polarized light,  $yxx$  and  $yyy$ . Opposite to the case of  $\text{BC}_2\text{N}$  analyzed in Sec. IV A, in this case  $\sigma^{yxx}$  is virtually null in the band-edge region while  $\sigma^{yyy}$  shows a step-like feature of height  $\sim 30 \mu\text{A}/\text{V}^2$ . Above  $E_{\Gamma Y} \sim 1.95$  eV, transitions along the  $\Gamma Y$  direction start to contribute [see Fig. 6(b)]; the dipole selection rule does not apply in this  $k$ -space region, hence  $\sigma^{yxx}$  becomes finite. Meanwhile,  $\sigma^{yyy}$  exhibits a second step at  $E_{\Gamma Y}$  but with opposite sign, hence diminishing the shift-current magnitude.

The dielectric function shown in Fig. 7(b) shares many of the properties of the shift current; the  $xx$  component is virtually null in the band-edge region and becomes finite

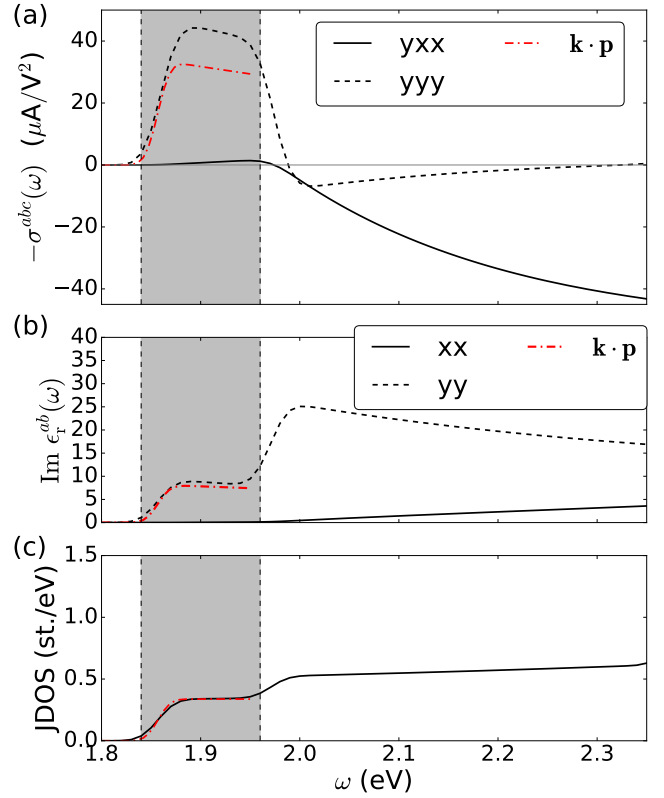


FIG. 7: (a) Shift-current spectrum, (b) imaginary part of the dielectric function, and (c) joint density of states of monolayer GeS. Black lines indicate *ab-initio* calculations, while the red lines depict the prediction of the two-band  $\mathbf{k} \cdot \mathbf{p}$  model. The grey area highlights the band-edge region from  $E_g \sim 1.85$  eV to  $E_{\Gamma Y} \sim 1.97$  eV.

at energies larger than  $E_{\Gamma Y}$ , while the  $yy$  component exhibits two step-like features, one at  $E_g$  and another one at  $E_{\Gamma Y}$ . The two steps present in both  $\sigma^{yyy}$  and  $\text{Im } \epsilon_T^{yy}$  are clearly inherited from the behavior of the JDOS, shown in Fig. 7(c).

## 2. Two-band model

In this section we construct a two-band  $\mathbf{k} \cdot \mathbf{p}$  model for monolayer GeS, along the same lines as the one in Sec. IV A 2 for monolayer  $\text{BC}_2\text{N}$ . We consider the valence and conduction bands at the band edge  $\Gamma$ , and apply quasi-degenerate perturbation theory to extract the expansion coefficients in Eq. (18). The corresponding band dispersion is shown in Fig. 6(a) as dashed lines, which shows a good quantitative agreement with the DFT results near the  $\Gamma$  point.

In Fig. 7 we show the model results for the optical properties and the JDOS in the band-edge region. The step-like feature of both the JDOS and the finite component of the dielectric function,  $\text{Im } \epsilon_T^{yy}$ , are quantitatively well described by the model throughout the whole band-

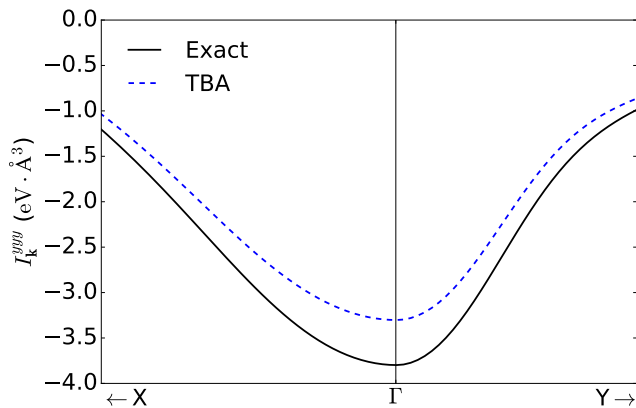


FIG. 8:  $k$ -resolved plot of the shift-current matrix-element of Eq. (25) for the  $yyy$  component in GeS, centered at the band edge  $\Gamma$ . The solid and dashed line denote the exact and diagonal TBA results, respectively.

edge region. Regarding the finite shift-current component,  $\sigma^{yyy}$ , the model underestimates the DFT value by  $\sim 20\%$ . While this discrepancy between model and exact results is significantly larger than the one found in the case of the JDOS and dielectric function, it is nevertheless much less severe when compared to the shift-current prediction in monolayer  $\text{BC}_2\text{N}$  in Sec. IV A 2, where we found a difference by a factor of 5.

### 3. Diagonal tight-binding approximation

The effect of the diagonal TBA on the optical properties of monolayer GeS was analyzed in Ref. [16], following the same procedure as the one here. Using 16 MLWFs in the basis set, it was found that the relative error entailed by the approximation was  $\sim 14\%$  for the shift-current component  $yyy$ . This value is in line with the information present in Fig. 8, which shows the effect of the diagonal TBA on the summed matrix elements [Eq. (25)] for the  $yyy$  component; the discrepancy at the band-edge is  $\sim 16\%$ , significantly lower than the same comparison in  $\text{BC}_2\text{N}$  for the basis with 16 MLWFs [see Fig. 5].

## V. DISCUSSION

We have performed an analysis of several electronic and optical properties of monolayer  $\text{BC}_2\text{N}$  and GeS, including the shift-current contribution to the BPVE. Part of our analysis has been based on *ab-initio* calculations performed within a recently developed approach based on the Wannier-interpolation of the shift current [16]. Our results have shown that the band-edge response encoded into both the dielectric function and the shift current is governed by dipole selection rules associated to the mirror parities of the band-edge states, which determines the

directionality of the optical properties [15, 35, 36]. Above the band-edge region, the peak shift-current response is rather large, on the order of other low-dimensional materials [12, 13].

We have further constructed a two-band  $\mathbf{k} \cdot \mathbf{p}$  model based on previous works [14, 18, 39]. For this purpose, we have extracted the relevant parameters from our *ab-initio* calculations by applying quasi-degenerate perturbation theory to the Wannier-based scheme. Our  $\mathbf{k} \cdot \mathbf{p}$  results have provided an accurate quantitative description of the band dispersion, JDOS and dielectric function near the band-edge region in both of the studied systems. In contrast, the  $\mathbf{k} \cdot \mathbf{p}$  prediction for the shift current has shown a significant deviation from the DFT results: it was off by nearly a factor 5 for  $\text{BC}_2\text{N}$ , while it entailed a much lower yet non-negligible relative error of  $\sim 20\%$  for GeS.

As a possible source of this discrepancy, we have performed a systematic analysis of the diagonal TBA; this amounts to discarding off-diagonal elements of the position operator, which is an implicit assumption of the tight-binding formulation. In first place, we have found that the effect of this approximation is much larger on the shift current than on the dielectric function, an indication of the strong wavefunction-sensitivity of the shift mechanism. Secondly, the quality of the  $\mathbf{k} \cdot \mathbf{p}$  model for the shift current seems to be intimately connected to the importance of the diagonal TBA in a given system. Thirdly, our analysis has revealed a marked dependence of the diagonal TBA on the size of the Wannier basis. Furthermore, the results do not converge monotonically, *i.e.*, the wavefunction-overlap giving rise to off-diagonal position matrix-elements does not always decrease with increasing basis-size. Therefore, the possibility of obtaining a well-converged calculation within the diagonal TBA seems not to be guaranteed.

In conclusion, the diagonal TBA produces a large effect on the shift current due to its strong sensitivity to wavefunction-properties. As a consequence, the use of  $\mathbf{k} \cdot \mathbf{p}$  models for quantitatively analyzing the shift current should be taken with care, even when the parameters are obtained via *ab-initio* methods.

*Acknowledgements* – We thank Stepan S. Tsirkin for sharing the `irrep` computer code that determines the mirror eigenvalues of the Bloch states [37], and for a previous collaboration on related work. This work was supported by Grant No. FIS2016-77188-P from the Spanish Ministerio de Economía y Competitividad.

## Appendix A: Model and $\mathbf{k} \cdot \mathbf{p}$

### 1. Quasi-degenerate (Löwdin) perturbation theory

Consider a Hamiltonian

$$H = H^0 + H' \quad (\text{A1})$$

where the eigenvalues  $E_n$  and eigenfunctions  $|n\rangle$  of  $H^0$  are known, and  $H'$  is a perturbation. In a nutshell,

quasi-degenerate perturbation theory assumes that the set of eigenfunctions of  $H^0$  can be divided into subsets  $A$  and  $B$  that are weakly coupled by  $H'$ , and that we are only interested in subset  $A$ . This theory asserts that a transformed Hamiltonian  $\tilde{H}$  exists within subspace  $A$  such that

$$\tilde{H} = \tilde{H}^0 + \tilde{H}^1 + \tilde{H}^2 + \dots \quad (\text{A2})$$

where  $\tilde{H}^j$  contain matrix elements of  $H'$  to the  $j$ th power. According to Appendix B of Ref 44, the first three terms are

$$\tilde{H}_{mm'}^0 = H_{mm'}^0, \quad (\text{A3})$$

$$\tilde{H}_{mm'}^1 = H'_{mm'}, \quad (\text{A4})$$

$$\tilde{H}_{mm'}^2 = \frac{1}{2} \sum_l H'_{ml} H'_{lm'} \left( \frac{1}{E_m - E_l} + \frac{1}{E_{m'} - E_l} \right) \quad (\text{A5})$$

where  $m, m' \in A$  and  $l \in B$ . The approximation  $\tilde{H} \sim \tilde{H}^0 + \tilde{H}^1$  amounts to truncating  $H$  to the  $A$  subspace. By further including  $\tilde{H}^2$ , the coupling to the  $B$  subspace is incorporated approximately, “renormalizing” the elements of the truncated matrix.

## 2. Application to Wannier-based $\mathbf{k} \cdot \mathbf{p}$ perturbation theory

Let us adopt the notation described in Sec. III.B of Ref. 28. We shift the origin of  $k$  space to the point where the band edge (or some other band extremum of interest) is located, and Taylor expand around that point the Wannier-gauge Hamiltonian,

$$H^{(W)}(\mathbf{k}) = H^{(W)}(0) + \sum_a H_a^{(W)}(0) k_a \quad (\text{A6})$$

$$+ \frac{1}{2} \sum_{ab} H_{ab}^{(W)}(0) k_a k_b + \mathcal{O}(k^3) \quad (\text{A7})$$

where  $a, b = x, y, z$ , and

$$H_a^{(W)}(0) = \left. \frac{\partial H^{(W)}(\mathbf{k})}{\partial k_a} \right|_{\mathbf{k}=0} \quad (\text{A8})$$

$$H_{ab}^{(W)}(0) = \left. \frac{\partial^2 H^{(W)}(\mathbf{k})}{\partial k_a \partial k_b} \right|_{\mathbf{k}=0} \quad (\text{A9})$$

We now apply to  $H^{(W)}(\mathbf{k})$  a similarity transformation  $U(0)$  that diagonalizes  $H^{(W)}(0)$ , and call the transformed Hamiltonian  $H(\mathbf{k})$ ,

$$H(\mathbf{k}) = \overbrace{H}^{H^0} + \overbrace{\sum_a \bar{H}_a k_a + \frac{1}{2} \sum_{ab} \bar{H}_{ab} k_a k_b}^{H'} + \mathcal{O}(k^3), \quad (\text{A10})$$

where we introduced the notation

$$\bar{\mathcal{O}} = U^\dagger(0) \mathcal{O}^{(W)}(0) U(0), \quad (\text{A11})$$

and applied it to  $\mathcal{O} = H, H_a, H_{ab}$ . We can now use the machinery of Sec. A1 by choosing the diagonal matrix

$\bar{H}$  as our  $H^0$ , and the remaining (nondiagonal) terms in Equation (A10) as  $H'$ . Collecting terms in Eq. (A2) up to second order in  $\mathbf{k}$  we get

$$\begin{aligned} \tilde{H}_{mm'}(\mathbf{k}) &= \bar{H}_{mm'} + \sum_a (\bar{H}_a)_{mm'} k_a \\ &+ \frac{1}{2} \sum_{a,b} [(\bar{H}_{ab})_{mm'} + (T_{ab})_{mm'}] k_a k_b + \mathcal{O}(k^3), \end{aligned} \quad (\text{A12})$$

where  $m, m' \in A$  and we have defined the virtual-transition matrix

$$\begin{aligned} (T_{ab})_{mm'} &= \sum_{l \in B} (\bar{H}_a)_{ml} (\bar{H}_b)_{lm'} \\ &\times \left( \frac{1}{E_m - E_l} + \frac{1}{E_{m'} - E_l} \right) = (T_{ab})_{m'm}^*. \end{aligned} \quad (\text{A13})$$

(The  $T_{ab}$  term in Eq. (A12) gives an Hermitean contribution to  $\tilde{H}(\mathbf{k})$  only after summing over  $a$  and  $b$ , whereas the other terms are Hermitean already before summing.)

## 3. Two-band case

Let us now specialize to the case where the subspace  $A$  of interest comprises only two bands. Then  $\tilde{H}(\mathbf{k})$  is a  $2 \times 2$  Hermitean matrix, and can be expanded as

$$\tilde{H}(\mathbf{k}) = \epsilon_0(\mathbf{k}) \mathbb{1} + \sum_i f_i(\mathbf{k}) \sigma_i \quad (i = x, y, z), \quad (\text{A14})$$

where  $\mathbb{1}$  is the  $2 \times 2$  identity matrix and  $\sigma_i$  are the three Pauli matrices. Using  $\text{Tr}(\sigma_i) = 0$  and  $\text{Tr}(\sigma_i \sigma_j) = 2\delta_{ij}$ , we find that the expansion coefficients are given by

$$\epsilon_0(\mathbf{k}) = \frac{1}{2} \text{Tr} [\tilde{H}(\mathbf{k})], \quad (\text{A15})$$

$$f_i(\mathbf{k}) = \frac{1}{2} \text{Tr} [\tilde{H}(\mathbf{k}) \cdot \sigma_i]. \quad (\text{A16})$$

The above quantities and their derivatives can be used to compute the shift-current and dielectric matrix-elements of a generic two-band model; these were expressed in Eqs. (22) and (23) of the main text and are repeated here for convenience

$$I_{\mathbf{k}\cdot\mathbf{p}}^{abc}(\omega) = \sum_{ijm} \frac{1}{4\epsilon^3} [(f_m f_{i,b} f_{j,ac} - f_m f_{i,b} f_{j,a} \frac{\epsilon_{,c}}{\epsilon}) \epsilon_{ijm} + (b \leftrightarrow c)] \quad (\text{A17})$$

$$K_{\mathbf{k}\cdot\mathbf{p}}^{ab}(\omega) = \sum_i \frac{4}{\epsilon^2} f_{i,a} f_{i,b} \quad (\text{A18})$$

with  $\epsilon = (\sum_i f_i f_i)^{1/2}$ ,  $\epsilon_{,a} = \partial_{k_a} \epsilon = \frac{1}{\epsilon} \sum_i f_i f_{i,a}$ ,  $f_{i,a} \equiv \partial_{k_a} f_i$  and  $f_{i,ab} \equiv \partial_{k_a} \partial_{k_b} f_i$ . To evaluate Eqs. (A17) and (A18) at the band edge  $\mathbf{k} = 0$ , we need

$$f_i(0) = \frac{1}{2} \text{Tr} [\bar{H} \cdot \sigma_i], \quad (\text{A19})$$

$$f_{i,a}(0) = \frac{1}{2} \text{Tr}_A [\bar{H}_a \cdot \sigma_i], \quad (\text{A20})$$

$$f_{i,ab}(0) = \frac{1}{2} \text{Tr}_A \left[ \frac{1}{2} (\bar{H}_{ab} + \bar{H}_{ba} + T_{ab} + T_{ba}) \cdot \sigma_i \right] \quad (\text{A21})$$

where  $\text{Tr}_A$  denotes a trace using the  $2 \times 2$  blocks of  $\overline{H}_{ab}$  and  $T_{ab}$  in the  $A$  sector, and the last two terms above are obtained inserting Eq. (A12) in Eq. (A16) and taking derivatives. Using  $\overline{H}_{ab} = \overline{H}_{ba}$  together with

$$\begin{aligned} \text{Tr}_A [T_{ba} \cdot \sigma_i] &= \text{Tr}_A [\sigma_i \cdot T_{ba}] = \\ \text{Tr}_A [(T_{ab} \cdot \sigma_i)^\dagger] &= (\text{Tr}_A [\sigma_i \cdot T_{ba}])^*, \end{aligned} \quad (\text{A22})$$

Eq. (A21) can be simplified to

$$f_{i,ab}(0) = \frac{1}{2} \text{Re} \text{Tr}_A \left[ \frac{1}{2} (\overline{H}_{ab} T_{ab}) \cdot \sigma_i \right] \quad (\text{A23})$$

The real quantities  $f_i(0)$ ,  $f_{i,a}(0)$  and  $f_{i,ab}(0)$  given by Eqs. A19, A20 and A23 are sufficient to evaluate the first term of the shift-current matrix element Eq. (A17) (the only nonzero term right at the band edge). As we move away from the band edge, the second term in this equation becomes nonzero.

- 
- [1] J. E. Spanier, V. M. Fridkin, A. M. Rappe, A. R. Akshayev, A. Polemi, Y. Qi, Z. Gu, S. M. Young, C. J. Hawley, D. Imbrenda, et al., *Nature Photonics* **10**, 611 (2016).
- [2] W. T. H. Koch, R. Munser, W. Ruppel, and P. Würfel, *Ferroelectrics* **13**, 305 (1976), URL <http://www.tandfonline.com/doi/abs/10.1080/00150197608236596>.
- [3] G. B. Osterhoudt, L. K. Diebel, M. J. Gray, X. Yang, J. Stanco, X. Huang, B. Shen, N. Ni, P. J. W. Moll, Y. Ran, et al., *Nature Materials* (2019), ISSN 1476-1122, 1476-4660.
- [4] J. Ma, Q. Gu, Y. Liu, J. Lai, P. Yu, X. Zhuo, Z. Liu, J.-H. Chen, J. Feng, and D. Sun, *Nature Materials* **18**, 476 (2019), ISSN 1476-4660, URL <https://doi.org/10.1038/s41563-019-0296-5>.
- [5] Y. Zhang, T. Holder, H. Ishizuka, F. de Juan, N. Nagaosa, C. Felser, and B. Yan, arXiv:1903.06264 [cond-mat] (2019).
- [6] Y. J. Zhang, T. Ideue, M. Onga, F. Qin, R. Suzuki, A. Zak, R. Tenne, J. H. Smet, and Y. Iwasa, **570**, 349 (2019), ISSN 1476-4687, URL <https://www.nature.com/articles/s41586-019-1303-3>.
- [7] M.-M. Yang, D. J. Kim, and M. Alexe, *Science* **360**, 904 (2018).
- [8] L. Z. Tan and A. M. Rappe, *Phys. Rev. Lett.* **116**, 237402 (2016), URL <https://link.aps.org/doi/10.1103/PhysRevLett.116.237402>.
- [9] T. Morimoto and N. Nagaosa, *Sci. Adv.* **2**, e1501524 (2016).
- [10] Y. Zhang, H. Ishizuka, J. van den Brink, C. Felser, B. Yan, and N. Nagaosa, *Phys. Rev. B* **97**, 241118 (2018), URL <https://link.aps.org/doi/10.1103/PhysRevB.97.241118>.
- [11] Z. Yan, arXiv:1812.02191 [cond-mat] (2018-12-05), 1812.02191, URL <http://arxiv.org/abs/1812.02191>.
- [12] S. Liu, F. Zheng, and A. M. Rappe, *J. Phys. Chem. C* **121**, 6500 (2017).
- [13] T. Rangel, B. M. Fregoso, B. S. Mendoza, T. Morimoto, J. E. Moore, and J. B. Neaton, *Phys. Rev. Lett.* **119**, 067402 (2017).
- [14] A. M. Cook, B. M. Fregoso, F. d. Juan, S. Coh, and J. E. Moore, *Nat. Commun.* **8**, 14176 (2017).
- [15] J. Ibañez-Azpiroz, I. Souza, and F. de Juan, arXiv:1906.07627 [cond-mat] (2019-06-18), 1906.07627, URL <http://arxiv.org/abs/1906.07627>.
- [16] J. Ibañez-Azpiroz, S. S. Tsirkin, and I. Souza, *Phys. Rev. B* **97**, 245143 (2018), URL <https://link.aps.org/doi/10.1103/PhysRevB.97.245143>.
- [17] C. Wang, X. Liu, L. Kang, B.-L. Gu, Y. Xu, and W. Duan, *Phys. Rev. B* **96**, 115147 (2017).
- [18] A. Bácsi and A. Virosztek, *Phys. Rev. B* **87**, 125425 (2013).
- [19] N. Marzari and D. Vanderbilt, *Phys. Rev. B* **56**, 12847 (1997).
- [20] I. Souza, N. Marzari, and D. Vanderbilt, *Phys. Rev. B* **65**, 035109 (2001).
- [21] V. M. Fridkin, *Crystallogr. Rep.* **46**, 654 (2001).
- [22] B. I. Sturman and V. M. Fridkin, *The photovoltaic and photorefractive effects in noncentrosymmetric materials* (Gordon and Breach, 1992), ISBN 978-2-88124-498-8.
- [23] E. L. Ivchenko and G. E. Pikus, *Superlattices and Other Heterostructures* (Springer, Berlin, 1997).
- [24] J. E. Sipe and A. I. Shkrebtii, *Phys. Rev. B* **61**, 5337 (2000).
- [25] N. Marzari, A. A. Mostofi, J. R. Yates, I. Souza, and D. Vanderbilt, *Rev. Mod. Phys.* **84**, 1419 (2012).
- [26] T. Yusufaly, D. Vanderbilt, and S. Coh, *Tight-Binding Formalism in the Context of the PythTB Package*, <http://physics.rutgers.edu/pythtb/formalism.html>.
- [27] J. R. Yates, X. Wang, D. Vanderbilt, and I. Souza, *Phys. Rev. B* **75**, 195121 (2007).
- [28] X. Wang, J. R. Yates, I. Souza, and D. Vanderbilt, *Phys. Rev. B* **74**, 195118 (2006).
- [29] G. Pizzi, V. Vitale, R. Arita, S. Blgel, F. Freimuth, G. Granton, M. Gibertini, D. Gresch, C. Johnson, T. Koretsune, et al., arXiv:1907.09788 [cond-mat, physics:physics] (2019), URL <http://arxiv.org/abs/1907.09788>.
- [30] P. Giannozzi, S. Baroni, N. Bonini, M. Calandra, R. Car, C. Cavazzoni, D. Ceresoli, G. L. Chiarotti, M. Cococcioni, I. Dabo, et al., *J. Phys.: Condens. Matter* **21**, 395502 (2009), URL <http://stacks.iop.org/0953-8984/21/i=39/a=395502>.
- [31] J. P. Perdew, K. Burke, and M. Ernzerhof, *Phys. Rev. Lett.* **77**, 3865 (1996).
- [32] A. A. Mostofi, J. R. Yates, Y.-S. Lee, I. Souza, D. Vanderbilt, and N. Marzari, *Comput. Phys. Commun.* **178**, 685 (2008).
- [33] Z. Pan, H. Sun, and C. Chen, *Phys. Rev. B* **73**, 193304 (2006), URL <https://link.aps.org/doi/10.1103/PhysRevB.73.193304>.
- [34] A. Y. Liu, R. M. Wentzcovitch, and M. L. Cohen, *Phys. Rev. B* **39**, 1760 (1989).
- [35] G. F. Bassani and G. P. Parravicini, *Il Nuovo Cimento*

- B **50**, 95 (1967).
- [36] G. F. Bassani, *Electronic states and optical transitions in solids*, (1975), [1st ed.] ed., ISBN 978-0-08-016846-3.
- [37] S. S. Tsirkin, <https://github.com/stepan-tsirkin/irrep>.
- [38] S. Fang, R. Kuate Defo, S. N. Shirodkar, S. Lieu, G. A. Tritsarlis, and E. Kaxiras, Phys. Rev. B **92**, 205108 (2015), URL <https://link.aps.org/doi/10.1103/PhysRevB.92.205108>.
- [39] X. Yang, K. Burch, and Y. Ran (2017), 1712.09363.
- [40] M. Graf and P. Vogl, Phys. Rev. B **51**, 4940 (1995).
- [41] J. Bennetto and D. Vanderbilt, Phys. Rev. B **53**, 15417 (1996).
- [42] I. Paul and G. Kotliar, Phys. Rev. B **67**, 115131 (2003).
- [43] T. B. Boykin, M. Luisier, and G. Klimeck, Eur. J. Phys. **31**, 1077 (2010).
- [44] R. Winkler, *Spin-orbit Coupling Effects in Two-Dimensional Electron and Hole Systems* (Springer, 2003), 2003rd ed., ISBN 978-3-540-01187-3.